Advances in Time-Dependent Monte Carlo Simulations for Void Velocity Determination Using Neutron Noise Techniques

Toshihiro Yamamoto[a*], Xiuzhong Shen[a], Hiroki Sakamoto[b]

[a]*Institute for Integrated Radiation and Nuclear Science, Kyoto University, 2 Asashiro Nishi, Kumatori-cho, Sennan-gun, Osaka, 590-0494, Japan*
[b]*Independent researcher, Radiation Dose Analysis and Evaluation Network, 4-13-14, Kokubunji-shi, Tokyo, 185-0001, Japan*

Abstract

Neutron noise measurements for estimating void velocity in a void-containing water flow where spherical bubbles move upward are simulated using a continuous energy Monte Carlo method. The method is newly equipped with a function for handling time-varying locations of void bubbles. In the simulations, time-series data of neutron counts in axially-placed detectors are obtained. The data are subsequently processed to yield the cross-correlation function (CCF), cross-power spectral density (CPSD), and auto power spectral density (APSD). The void velocities are estimated from the maximum CCF, slope of the phase of the CPSD as a function of frequency, and dip frequency of the APSD. These three methods yield a constant void velocity estimation. The simulations demonstrate that the noise techniques are insensitive to a void flow that contains smaller bubbles.

Keywords: Void velocity; Neutron noise; Monte Carlo; Simulation

1. Introduction

To enhance the safety and reliability of boiling water reactor operations, the development of determining void-related information, such as local void fraction and void velocity, has long been pursued based on various measurement techniques. Many studies have focused on

* Corresponding author. Tel: +81 72 451 2414; Fax: +81 72 451 2658
E-mail: yamamoto.toshihiro.8u@kyoto-u.ac.jp (T. Yamamoto)

techniques using neutron noise to measure two-phase flow properties in void-containing coolants/moderators (Kosály, 1980; Kosály et al., 1982; Pázsit and Demazière, 2010; Pázsit and Dykin, 2010; Loberg et al., 2010; Dykin and Pázsit, 2013). The diagnostic methods of BWRs that use in-core monitors (e.g., local power range monitors, traversing in-core probes, and self-powered neutron detectors) are considered advantageous because of their non-intrusive nature for measuring void-related information (Van der Hagen and Hoogenboom, 1988). For example, the void transit time in the channel of a BWR is expected to be measured using the cross-power spectral density (CPSD) of neutron noise between axially-placed detector pairs.

A reliable theory that derives void-related information such as the local void velocity and void fraction profile from the auto power spectral density (APSD) and CPSD has not been fully established hitherto. To make progress in research on this subject, an experimental project intended to validate the theoretical models was undertaken in a zero-power critical assembly CROCUS at the École Polytechnique Fédérale de Lausanne (EPFL) (Hursin et al., 2019; Hursin et al., 2020). As a first campaign in the project, the void velocity or void transit time was successfully acquired using the neutron noise measured in CROCUS.

In addition to the experimental studies, a numerical Monte Carlo simulation is a useful method to supplement the knowledge that cannot easily be obtained in actual experiments. In numerical simulations, many combinations of several void-related parameters are possible, and the results are free from experimental noise, which helps us understand the true nature of void velocity measurements. There have been some attempts to use Monte Carlo simulations in which neutron noise techniques for determining void-related information have been performed (Pázsit et al., 1984; Dykin and Pázsit, 2013; Yamamoto, 2014; Pettersen et al., 2015; Yamamoto and Sakamoto, 2016; Yamamoto, 2017; Yamamoto and Sakamoto, 2021). Monte Carlo simulations can be classified mainly into two types: one is to solve the frequency domain neutron noise equation using complex-valued particle weights that represent the

neutron noise (Yamamoto, 2014; Yamamoto and Sakamoto, 2016; Rouchon et al., 2017; Yamamoto and Sakamoto 2021), and the other is a time-dependent neutron transport simulation in void-containing water flow (Yamamoto 2017). The simulations of the latter were performed in a two-dimensional rectangular geometry with three energy group constants. The APSDs and cross-correlation functions (CCF) of neutron noise were obtained in the simulations. Therefore, the completeness of the simulations was limited by the multigroup approximation and simplified geometry.   The time-dependent approach has resemblance to the works done by using time-series data from deterministic reactor dynamics codes (e.g., DYN3D (Rohde et al., 2018; Viebach et al., 2019), FEMFFUSION (Vidal-Ferràndiz et al., 2020)) for neutron flux fluctuations in a power reactor. More realistic simulations using a production-level continuous energy Monte Carlo code would enable us to handle detailed three-dimensional geometry and faithfully reproduce realistic neutron transport phenomena in void-containing water flow. However, no existing production-level Monte Carlo code can perform time-dependent Monte Carlo simulations for void-containing water flow because the geometry continuously changes during the simulations. Although a Monte Carlo algorithm that can handle time-varying locations of void bubbles has been developed by Yamamoto (2017), it was implemented in an in-house research-purpose code and thus is inaccessible.

From such circumstances, the first step of this study is to implement Yamamoto's (2017) algorithm into a continuous energy Monte Carlo code, MCNP (Briesmeister, 1997). Subsequently, using the modified code, neutron noise simulations were performed for void-containing water flow. Three noise methods were chosen for determining void velocity: the CCF method, CPSD method, and APSD method (Kosály and Meskó, 1976). The feasibility and applicability of the three methods are discussed from the viewpoint of how precisely the void velocity can be reproduced based on neutron noise techniques.

In Section 2, the neutron noise techniques adopted in this study for determining the void velocity in void-containing water flow are briefly reviewed. In Section 3, the Monte Carlo

3

1 simulation method implemented in the continuous energy Monte Carlo code is presented. In

2 Section 4, Monte Carlo simulations that were performed for void velocity determination in

3 void-containing water flow are presented to demonstrate that fundamental properties can be

4 determined through numerical simulations. Finally, Section 5 summarizes the study and

5 outlines the main conclusions.

6

2. Neutron noise techniques for determining void velocity

8   The neutron noise techniques adopted in this study for determining void velocity were the

9 CCF, CPSD, and APSD methods. Suppose that at least two neutron detectors are aligned along

10 the direction of the void-containing water flow. The neutron detectors would count neutrons

11 that penetrate the void-containing water flow region. The CCF method obtains the CCF

12 between two detectors positioned at z_1 and z_2 using the following equation:

$$CCF_{12}(z_1, z_2, \tau) = \int_{-\infty}^{+\infty} \left(X_1(t) - \overline{X_1(t)}\right)\left(X_2(t - \tau) - \overline{X_2(t)}\right)dt, \tag{1}$$

14 where t is the time; the lag τ is the size of the time shift; $X_1(t)$ and $X_2(t)$ are the detector

15 signals of the two detectors; and $\overline{X_1(t)}$ and $\overline{X_2(t)}$ are the means of $X_1(t)$ and $X_2(t)$,

16 respectively. The void transit time between the two detectors can be determined by the

17 maximum of $CCF_{12}(z_1, z_2, \tau)$ outside the origin $\tau = 0$.

18   Using CCF_{12}, the one-sided CPSD is obtained by Fourier transformation as follows:

$$CPSD(z_1, z_2, \omega) = 2\int_{-\infty}^{+\infty} CCF_{12}(\tau)e^{-i\omega\tau}d\tau$$

$$= 2\int_{0}^{+\infty} CCF_{12}(z_1, z_2, \tau)e^{-i\omega\tau}d\tau + 2\int_{0}^{+\infty} CCF_{21}(z_2, z_1, \tau)e^{-i\omega\tau}d\tau, \tag{2}$$

21 where i is the imaginary unit, and ω is the angular frequency where $0 < \omega \le +\infty$ (Uhrig,

22 1970). Because of the propagating nature of the water density perturbation along the flow

23 direction, the CPSD in Eq. (2) can be rewritten as follows (Kosály, 1980):

$$CPSD(z_1, z_2, \omega) = APSD(z_1, \omega)\exp(-i\omega\tau_{12}), \tag{3}$$

25 where $APSD(z_1, \omega)$ is the APSD at position z_1, and τ_{12} is the void transit time between

26 the positions at z_1 and z_2. The CPSD phase is given as follows:

$$\theta = \tan^{-1}\left(\frac{\text{Im}[CPSD(z_1, z_2, \omega)]}{\text{Re}[CPSD(z_1, z_2, \omega)]}\right), \tag{4}$$

where Im[x] and Re[x] are the imaginary and real parts of a complex value x, respectively.

Using the θ values at several frequency points, the void velocity can be obtained as follows:

$$V = (z_2 - z_1)\frac{\omega}{\theta}, \tag{5}$$

where θ/ω is obtained by linearly fitting the slope of phase θ as a function of ω at several frequency points.

The neutron noise detected by an in-core monitor consists of two components: the "local component" and the "global component" (Behringer, 1977). The "local component" is caused by the local fluctuation of water density near the neutron detector. The "global component" is caused by the overall reactivity change of the reactor and other long-range space-dependent components that deviate from point kinetics. This study focuses on the "local component." The smaller the detector, the more precisely local information can be detected. Yamamoto (2017) demonstrated that an APSD of an axially long single detector can be used to detect void velocity. Here, we consider a neutron detector with an active length L in the axial direction. The APSD of the local component obtained by this detector is given as follows (Kosály and Meskó, 1976):

$$APSD(\omega) \propto H_n(\omega)H_d(\omega), \tag{6}$$

$$H_n(\omega) = \frac{1}{(1 + \omega^2 \tau_n^2)^2}, \tag{7}$$

$$\tau_n = \frac{1}{\mu V}, \tag{8}$$

$$H_d(\omega) = \frac{\sin^2(\omega \tau_d)}{(\omega \tau_d)^2}, \tag{9}$$

$$\tau_d = \frac{L}{2V}, \tag{10}$$

where V is the void velocity in the axial direction, and μ is the spatial decay constant of the local component. If a sufficiently short detector is used and the void velocity is relatively high, $H_d(\omega)$ is almost independent of the frequency within the frequency range of interest. In such

5

a situation, the void velocity and void fraction can be deduced from the break frequency of $H_n(\omega)$, $1/\tau_n$. However, this method requires neutronics calculations to estimate the spatial decay constant μ. On the other hand, as long as the detector is not short and the void velocity is not very high, $H_d(\omega)$ exhibits clear dips at the frequencies $\omega_n = 2n\pi V/L$ ($n = 1, 2, \ldots$). Once the frequency of a dip is known, the void velocity can be determined as follows:

$$V = \frac{\omega_n L}{2\pi n}, \qquad n = 1, 2, \ldots, \tag{11}$$

where ω_n is the angular frequency of the nth dip. If the detector is short or the void velocity is high, the dips appear in the high frequency region where the white noise is dominant, and the dips are indiscernible from the white noise. This study considers the situation where the APSD is dominated by $H_d(\omega)$, and the dips are clearly observed. The method based on $H_d(\omega)$ is superior to the method based on $H_n(\omega)$ because it does not require the estimation of any neutronics parameters. In an operating BWR, the first dip would fall over 100 Hz because of the higher void velocity, which makes the first dip indiscernible. Nevertheless, this study tries to demonstrate the feasibility of this method via numerical simulations.

3. Monte Carlo simulation for neutron noise

This section describes the Monte Carlo calculation method for simulating neutron noise measurements in a void-containing water flow. Recently, the development of time-dependent Monte Carlo methods has been promoted mainly for reactor kinetics analyses. While these time-dependent methods are employed with a fixed geometry, neutron noise analyses for void-containing water flow must be performed with a time-varying geometry. In Yamamoto's study (2017), time-varying geometry modeling was implemented in an in-house research-purpose multigroup Monte Carlo code. For this study, the special function for a time-varying geometry was implemented in a continuous energy Monte Carlo code MCNP 4C (Briesmeister, 2000). Although the Monte Carlo algorithm used in this study is similar to that in Yamamoto's study, it is presented below.

1 (1) Fig. 1 shows the configuration for modeling a void-containing water flow and a neutron

2 detection system. The geometry was composed of a void-containing water flow region, water

3 region with full water density, and neutron detectors. Isotropic neutrons were emitted from

4 the left end of the void flow region, and neutrons were detected by ^{3}He counters attached to

5 the right end of the void flow region. More details on this system are presented in Section 4.

6 [Fig.1]

7

8 (2) Before starting the random walk process of the neutrons, the positions of the void bubbles

9 are determined. The void bubbles were assumed to be spherical and all identical in diameter,

10 velocity, and direction (upward). A void bubble is randomly and uniformly allocated in the

11 void flow region, one by one, using pseudo-random numbers. If a void bubble overlaps the

12 bubbles already allocated, it is rejected, and a new position is determined. The number of void

13 bubbles in the void flow region is determined such that the total volume of the void bubbles

14 corresponds to the void fraction. Finally, a "void map" that is composed of three-dimensional

15 void positions is prepared for the subsequent Monte Carlo simulation.

16 (3) From the left end of the void flow region, a neutron is emitted isotropically at $t = t_0$. The

17 time t_0 coincides with the starting time of a data block for neutron counting. Each data block

18 in this study was composed of $M = 2^{14} = 16384$ time bins, each of which recorded the number

19 of neutron absorptions by each ^{3}He counter. The width of each time bin (i.e., sampling

20 interval) was $\Delta = 2 \times 10^{-4}$ s. This study employed an "analog Monte Carlo" method to

21 faithfully represent a realistic neutron noise measurement. Hence, the implicit capture and

22 Russian roulette were turned off. The particles were killed only when they escaped from the

23 external boundary or were absorbed. The position of the starting neutron is sampled uniformly

24 from the left surface of the void flow region. The energy of the starting neutron is sampled

25 from the neutron spectrum, as described in Section 4.

26 (4) The particle tracing in this study adopted the Woodcock delta tracking method for efficient

27 free path sampling in heterogeneous media (Woodcock, 1965). In the void flow region, the

free flight distance s to the next collision point is determined by

$$s = -\frac{\ln \xi_1}{\Sigma_t}, \tag{12}$$

where Σ_t is the total cross-section of light water, and ξ_1 is a pseudo-random number between 0 and 1. The elapsed time taken for this flight is $t_s = s/v$, where v is the velocity of the neutron. Each time the particle flies by its free flight distance, the positions of all void bubbles are shifted upward by $t_s V$, where V is the void velocity in the upward direction (although this shift is negligible compared to the neutron flight distance). Further, the distances between the collision point and the centers of all void bubbles are compared with the radius of the void bubbles. If one of the distances is shorter than the radius, the collision point is determined to be within a void bubble and the particle continues to fly with no changes in direction or energy. Subsequently, the next free flight distance is calculated again according to Eq. (12). If all distances are longer than the radius, the collision is regarded as a true collision with light water.

However, this algorithm is very inefficient because the comparison must be performed as many times as the number of void bubbles. To reduce the number of comparisons, the entire void flow region is discretized into several number of cells. Each void bubble is assigned to one of the cells in which its center is located. A void bubble that intersects with adjoining cells is assigned to the adjoining cells, as well as to the cell, where its center is located. Therefore, when a collision point is determined, the cell to which the collision point belongs is determined. Subsequently, the comparisons are performed only with the void bubbles assigned to the cell, thereby omitting the comparisons with the void bubbles not assigned to the cell. This algorithm can drastically reduce the number of comparisons.

(5) The random walk process of the particle continues until it escapes from the external boundary or is absorbed. When the particle is absorbed in the detector region at time t, a count is added to the mth time bin, where

$$m = \text{Int}\left[\frac{t}{\Delta}\right] + 1, \qquad (13)$$

and Int[x] denotes the largest integer that does not exceed x. If $m > M$, the count is discarded.

(6) After a particle is killed by an escape or absorption, the next source particle is emitted. Assuming that the timing of the source neutron emission follows the Poisson process, the time of the next starting neutron t_0 is updated as follows:

$$t_0' = t_0 - \frac{\ln \xi_2}{S}, \qquad (14)$$

where S is the number of source particles per unit time, and ξ_2 is another pseudo-random number between 0 and 1. Before starting the source neutron, the void map is updated so that the positions of all void bubbles are shifted upward by $(t_0' - t_0)V$. Repeat steps (3)–(5) until t_0 exceeds the end of the data block, $M\Delta$.

(7) Using the detector time response that is accumulated in the data block, the circular autocorrelation and cross-correlation functions are calculated using the following discrete form of Eq. (1):

$$C_{ij}(m\Delta) = \sum_{k=0}^{M-1} \left(x_{i,k} - \overline{x_{i,k}}\right)\left(x_{j,m+k} - \overline{x_{j,k}}\right), \qquad (15)$$

where $x_{i,k}$ represents the counts in the kth time bin of the detector i, and $\overline{x_{i,k}}$ denotes the mean value of $x_{i,k}$ over the data block. If $i = j$, then C_{ij} is an autocorrelation function (ACF). Otherwise, C_{ij} is a CCF. Using the ACF in Eq. (15), the APSD is calculated in discretized form as follows (Valentine and Mihalczo, 1996; Yamamoto, 2015; Talamo et al., 2019):

$$APSD(\omega_k) = 4\left[C_{ii}(0) + \sum_{m=0}^{M-1} C_{ii}(m\Delta)\cos(\omega_k m\Delta)\right], \qquad (16)$$

where $\omega_k = 2\pi k/(\Delta M)$ and $k = 0, 1, ..., M/2$. In the same manner, the CPSD is calculated as follows:

$$\text{Re}[CPSD(\omega_k)] = 2\left[\sum_{m=0}^{M-1} C_{ij}(m\Delta)\cos(\omega_k m\Delta) + \sum_{m=0}^{M-1} C_{ji}(m\Delta)\cos(\omega_k m\Delta)\right], \qquad (17)$$

$$\text{Im}[CPSD(\omega_k)] = 2\left[\sum_{m=0}^{M-1} C_{ji}(m\Delta)\sin(\omega_k m\Delta) - \sum_{m=0}^{M-1} C_{ij}(m\Delta)\sin(\omega_k m\Delta)\right], \quad (18)$$

where $\text{Re}[x]$ and $\text{Im}[x]$ denote the real and imaginary parts of x, respectively.

(8) The latest estimates of CCFs, APSDs, and CPSDs are averaged with the previous estimates. The data blocks are cleared. Return to step (3).

(9) Steps (3)–(8) are repeated until the desired statistics are obtained.

4. Monte Carlo simulation results

4.1 Model for simulations

Monte Carlo simulations using the MCNP 4C code were performed for the geometry shown in Fig. 1. The light water density was maintained at 20 °C and at atmospheric pressure. The horizontal dimension of the void-containing water flow channel was 4.6×4.6 cm, which was the same as the experiments performed in EPFL (Hursin et al., 2019; Hursin et al., 2020). The gap distance between the detectors, G, varied. The void velocity, void fraction, and diameter of the void bubbles were determined according to the EPFL experiments, as explained below.

Hursin et al. (2019) measured the gas velocity in an air–water two-phase flow in a vertical square duct with a cross-section of 4.6×4.6 cm and a height of 65.0 cm by using neutron noise techniques. As shown in Fig. 6 of Hursin et al.'s study (2019), the average void fraction, α, was obtained by utilizing the linear relationship between the average void fraction and the gas velocity where the air volumetric flow rates changed from 2 L/min to 100 L/min in the square duct. The present study determined the average bubble diameter (d_B) according to the following equation:

$$d_B = \frac{6\alpha}{a_i}, \quad (19)$$

where a_i is the interfacial area concentration, defined as the interfacial area per unit volume of the two-phase flow mixture. The a_i correlation of Akita and Yoshida (1974) was selected

10

here and is given as follows:

$$a_i = \frac{g^{0.6} D_H^{0.3}}{3 v_f^{0.2}} \left(\frac{\sigma}{\rho_f}\right)^{-0.5} \alpha^{1.13}, \tag{20}$$

where g, D_H, σ, v_f, and ρ_f, are the gravitational acceleration (m/s^2), hydraulic equivalent

diameter of the flow channel (m), surface tension (N/m), liquid kinematic viscosity (m^2/s),

and liquid density (kg/m^3), respectively. The predicted d_B values chosen in the simulations

were 0.910 cm and 0.809 cm. The former diameter, $d_B = 0.910$ cm, corresponded to the

injected air volumetric flow rate of 6.10 L/min. The estimated gas velocity V_g and average

void fraction α for $d_B = 0.910$ cm were 77.5 cm/s and 0.0531, respectively. The latter

diameter, $d_B = 0.809$ cm, corresponded to a flow rate of 25.0 L/min. The estimated gas

velocity and average void fraction for $d_B = 0.809$ cm were 129.6 cm/s and 0.132,

respectively. These predicted d_B values are in accordance with the average bubble sizes

measured using multi-sensor probes in the general upward air–water two-phase flows under

similar flow conditions in the vertical channel experiments of Shen et al. (2015). The

generation of new bubbles within a flow channel, axially increasing void velocity, and

nonuniform bubble diameters were not considered in this study. However, they can be easily

implemented in the present model. On the other hand, the modeling of bubble coalescence

and non-spherical bubble geometry is not straightforward and it would need a special

technique.

The pointwise nuclear data used in this study were based on the nuclear data library

JENDL-4 (Shibata et al., 2011). Since the calculations in this study were time-consuming, the

rectangular detector region whose dimensions were 4.6 cm in thickness, 5.0 cm in width, and

5.0 cm in height was filled with high density ^{3}He gas at 30 atm to increase the detector

efficiency. The pressure of the detector was the highest installed in the Spallation Neutron

Source at the Oak Ridge National Laboratory (Berry, 2016). Whereas the thickness and width

1 of the detector may affect the detection efficiency, these dimensions would not essentially

2 affect the final result except for the statistical uncertainty.

3   In this study, we assumed that the void velocity was measured in the reflector region of

4 a light water moderated reactor in the same way as the experiments in the EPFL. The spectrum

5 of the source neutrons, which were emitted into the void-containing water flow channel, was

6 calculated in the light water reflector region of the Tank-type Critical Assembly (TCA) at the

7 former Japan Atomic Energy Research Institute (Tsuruta et al., 1978), and the spectrum is

8 shown in Fig. 2. The neutron source intensity was 8×10^7 n/s.

9   [Fig. 2]

10 4.2 CPSD method

11   Using the Monte Carlo simulation method developed in this study, the CPSDs between

12 the axially-placed detectors were calculated for two void conditions: one was $d_B = 0.910$ cm,

13 $V_g = 77.5$ cm/s, and $\alpha = 0.0531$ (referred to as "Case 1"), and the other was $d_B = 0.809$ cm, V_g

14 $= 129.6$ cm/s, $\alpha = 0.132$ (referred to as "Case 2").

15   Figs. 3 and 4 show the phase θ as a function of the frequency for Case 1 and 2,

16 respectively. The gap distance G between the detectors was 5 cm, which means that the center-

17 to-center distance was 10 cm for the detector combinations D1-D2 and D2-D3 and 20 cm for

18 D1-D3. These center-to-center distances were used for the distance $(z_2 - z_1)$ in Eq. (5) when

19 the void velocities were calculated. In addition, calculations were performed for the gap

20 distance $G = 10$ cm for Case 2 in order to study the dependence on the gap distance. The

21 velocities obtained from a linear fitting of the slope are listed in Table 1. The errors in the

22 tables are based on the standard errors of the coefficients from the linear regressions. The void

23 velocities obtained from the CPSDs agreed with the true velocities within the errors regardless

24 of the gap distance. As seen in Figs. 3 and 4, the linear behavior of the phase with respect to

25 the frequency can be observed. The linearity of the phase in Case 1 was better than that in

26 Case 2. This difference may have been caused by the bubble diameter. As suggested by

Yamamoto (2017), a smaller bubble size may lead to a weaker signal correlation between the detectors. This weaker signal correlation can be understood by assuming a void-containing water flow with an infinitely small bubble size that makes no correlation between two detectors. To demonstrate this property, a simulation where the bubble diameter d_B was reduced from 0.910 cm to 0.4 cm was performed in Case 1. The parameters remained unchanged, except for the diameter. The phase as a function of frequency is shown in Fig. 5. The linearity of the phase was inferior to that of larger diameters. The void velocities obtained from the CPSDs for d_B = 0.4 cm are shown in row 4 of Table 1. The errors of the velocities were very large, which supports the idea that the performance of the neutron noise technique is reduced for a water flow containing small bubbles. This inferior linearity is caused by the lack of the computation time with respect to the time that would be required to obtain a satisfactory linearity. The linearity would be improved by using more computation time.

[Figs. 3, 4, 5][Table 1]

4.3 CCF method

The CCFs were calculated using the same time-series data used for the CPSDs in the previous section. The CCF of Case 1 as a function of the lag τ is shown in Fig. 6(a). The fluctuations of the CCF in Fig. 6(a) were smoothed out by taking a moving average, thereby making it easy to find the maximum CCF. The moving average was obtained by averaging 100 time-series data points before and after each data point, as shown in Fig. 6(b). Fig. 6(c) shows that the moving average of the CCF fitted properly to a quadratic function. The void velocities obtained from the maximum point of the quadratic function are listed in Table 2. Comparing the results in Tables 1 and 2, both CPSD and CCF yielded consistent void velocities with somewhat similar uncertainties.

[Figs. 6(a), 6(b), 6(c)][Table 2]

4.4 APSD method

The APSD method for determining void velocity was applied to the void condition Case 1 (d_B = 0.910 cm, V_g = 77.5 cm/s, and α = 0.0531). Since the dips of APSD appear at

1 frequencies $\omega_n = 2n\pi V/L \ (n = 1, 2, ...,)$ as described in Section 2, the dip frequencies

2 increase with the reduction in detector active length L. If a short detector was used, the dips

3 would be masked by the white noise of the APSD, which is dominant in the higher frequency

4 range. On the other hand, if a long detector was used, dips would appear in the low-frequency

5 range where the frequency resolution is relatively coarse. Every data point of the APSD is

6 located at $\omega_m = 2\pi m/(\Delta M) \ (m = 1, 2, ...,)$, where Δ is the sampling interval, and M is

7 the number of points per data block. The dip frequency ω_n generally does not coincide with

8 the dip frequency of the APSD ω_m because ω_m is defined at a discrete point. The relative

9 difference between ω_n and ω_m is given by

$$\frac{|\omega_n - \omega_m|}{\omega_n}, \quad m = n = 1, 2, ..., \tag{21}$$

11 which increases in the low-frequency range. Consequently, both too short and too long

12 detectors are not suitable for the APSD method for the reasons mentioned above. The detector

13 length must be determined such that the dip frequencies fall within the optimal frequency

14 range.

15   Noise simulations for determining void velocity were performed with detector lengths of

16 $L = 20$, 40, and 70 cm. The sampling interval was increased to $\Delta = 4 \times 10^{-4}$ s from the previous

17 sections to narrow the frequency interval and increase the frequency resolution. The calculated

18 APSDs for $L = 20$, 40, and 70 cm are shown in Figs. 7, 8, and 9, respectively. The function

19 $H_d(\omega)$, which indicates the dip frequencies, is also shown in those figures. Although the

20 lowest theoretical dip frequency for $L = 20$ cm is 3.875 Hz (77.5 (cm/s)/20 (cm)), the dip is

21 not observed in Fig. 7. The APSD around the lowest dip frequency was comparable to the

22 white noise. Thus, the detector length $L = 20$ cm was not sufficient for the APSD method. The

23 lowest dip frequencies of the APSDs for $L = 40$ and 70 cm were found at 1.984 Hz and 1.068

24 Hz, respectively. The lowest dip frequencies of $H_d(\omega)$ for $L = 40$ and 70 cm were 1.938 Hz

25 and 1.107 Hz, respectively, which closely coincided with the results of the APSD. The dips

26 beyond the second lowest frequency cannot be identified because of the interference from the

14

white noise. The velocities obtained from the dip frequencies and Eq. (11) were 79.4 cm/s and 74.8 cm/s for $L = 40$ and 70 cm, respectively. The differences in the estimated void velocities and the reference velocity (77.5 cm/s) may be attributed to the limited frequency resolution of the APSDs. A detector with a length of 40 cm was considered suitable for this numerical example.

[Figs. 7, 8, 9]

5. Conclusions

Neutron noise Monte Carlo simulations for void-containing water flow require the capacity of handling time-varying geometry. The simulations were already performed for a two-dimensional geometry with a multigroup in-house Monte Carlo code. In this study, the Monte Carlo algorithm was implemented in a production-level continuous energy Monte Carlo code. Owing to this advancement, more realistic and reliable neutron noise simulations could be performed to acquire more comprehensive knowledge of neutron noise measurements in void-containing water flow while performing actual experiments.

In this study, three methods—the CPSD, CCF, and APSD methods—were applied to simulate neutron noise measurements performed in an experimental facility of the EPFL. Throughout this study, the void bubbles were all assumed to be spherical and identical in diameter, velocity, and direction (upward). Both the CPSD and CCF methods yielded consistent results for the void velocities. Monte Carlo simulations revealed that the neutron noise techniques were less sensitive to water flow containing a smaller size of void bubbles and statistically significant results were not obtained.

The Monte Carlo simulations in this study demonstrated the feasibility of the APSD method, which used a relatively long single detector, although this method cannot be straightforwardly applied to an operating power reactor because of the reason stated in Section 2. The dip frequency of the APSD, which is related to the void velocity and detector length, could be identified with a detector whose length is properly chosen. A short detector makes

15

the dip frequency indiscernible from the white noise in the higher frequency range. A longer detector makes the dip frequency appear in the low-frequency range, where the frequency resolution is not sufficient for accurately determining the void velocity. To the best of the authors' knowledge, there have been no experiments aimed at measuring the first dip for determining the void velocity thus far. Performing the experiment would be desirable in the future.

Future works should include extending the capability of the Monte Carlo simulation method so that it can be applied to more realistic void-containing flows such as nonuniform void velocity profiles and other flow regimes, except bubbly flow. They should also investigate methods to improve the efficiency and viability of handling void flows containing small bubbles. The application of the proposed noise methods to a void-containing flow with axially varying void velocity would be an interesting topic that is worthy of studying as future work.

CRediT authorship contribution statement

Toshihiro Yamamoto: Supervision, Methodology in neutronics, Conceptualization, Investigation, Writing - original draft. **Xiuzhong Shen**: Methodology in thermal hydraulics, Writing. **Hiroki Sakamoto**: Software, Validation, Formal analysis, Data curation, Writing - review & editing.

References

Akita, K., Yoshida, F., 1974. Bubble size, interfacial area, and liquid-phase mass transfer coefficient in bubble columns. Ind. Eng. Chem. Process Des. Dev. 13, 84−91. https://doi.org/10.1021/i260049a016.

Behringer, K., Kosály, G., Kostić, L., 1977. Theoretical investigation of the local and global components of the neutron-noise field in a boiling water reactor. Nucl. Sci. Eng. 63, 306−318. https://doi.org/10.13182/NSE77-A27042.

1 Berry, K., 2016. Neutron lifecycle series: Helium-3 gas detectors at the SNS and HFIR

2 [online].https://conference.sns.gov/event/56/attachments/64/192/Lecture_6a-

3 _Neutron_Detection_with_He3_-_Kevin_Berry.pdf.

4 Briesmeister, J.F., Ed. 2000. MCNP—A General Monte Carlo N-particle transport code,

5 version 4C. LA-13709-M.

6 Dykin, V., Pázsit, I., 2013. Simulation of in-core neutron noise measurements for axial void

7 profile reconstruction in boiling water reactors, Nucl. Technol. 183, 354−366.

8 https://doi.org/10.13182/NT13-A19424.

9 Hursin, M., Pakari, O., Perret, G., Frajtag, P., Lamirand, V., Pázsit, I., Dykin, V., Por, G.,

10 Nylén, H., Pautz, A., 2019. Measurement of the gas velocity in a water-air mixture in

11 CROCUS using neutron noise technique. Proceedings of M&C 2019, Aug 25−29, Portland,

12 (OR) 2019.

13 Hursin, M., Pakari, O., Perret, G., Frajtag, P., Lamirand, V., Pázsit, I., Dykin, V., Por, G.,

14 Nylén, H., Pautz, A., 2020. Measurement of gas velocity in a water-air mixture in

15 CROCUS using neutron noise techniques. Nucl Technol. 206, 1566−1583.

16 https://dx.doi.org/10.1080/00295450.2019.1701906.

17 Kosály, G., Meskó, L., 1976. Theory of auto-spectrum of the local component of power-

18 reactor noise, Ann. Nucl. Energy 3, 233−236. https://doi.org/10.1016/0306-

19 4549(76)90084-0.

20 Kosály, G., 1980. Noise investigations in boiling water and pressurized-water reactors, Prog.

21 Nucl. Energy 5, 145−199. https://doi.org/10.1016/0149-1970(80)90004-9.

22 Kosály, G., Albrecht, R.W., Crowe, R.D., Dailey, D.J., 1982. Neutronic response to two-phase

23 flow in a nuclear reactor, Prog. Nucl. Energy 9, 22−36. https://doi.org/10.1016/0149-

24 1970(82)90027-0.

25 Loberg, J., Österlund, M., Blomgren, J., Bejmer, K., 2010. Neutron detection-based void

26 monitoring in boiling water reactors, Nucl. Sci. Eng. 164, 69-79. https://

17

doi.org/10.13182/NSE09-17.

Pázsit, I., Antonopoulos-Domis, M., Glöckler, O., 1984. Stochastic aspects of two-dimensional vibration diagnostics. Prog. Nucl. Energy 14, 165−196. https://doi.org/10.1016/0149-1970(84)90014-3.

Pázsit, I., Demazière, C., 2010. Noise techniques in nuclear systems. In: Cacuci, D.G., Ed., Handbook of Nuclear Engineering, Vol.3, 1629-1737, Springer.

Pázsit, I., Dykin, V., 2010. Investigation of the space-dependent noise induced by propagating perturbations, Ann. Nucl. Energy 37, 1329−1340. https://doi.org/10.1016/j.anucene.2010.05.014.

Pettersen, E.E., Demazière, C., Jareteg, K., Schönfeldt, T., Nonbøl, E., Lauritzen, B., 2015. Development of a Monte-Carlo based method for calculating the effect of stationary fluctuations, Proc. M&C+SNA+MC 2015, Nashville, TN, USA, Apr. 19-23, 2015.

Rohde, U., Seidl, M., Kliem, S., Bilodid, Y., 2018. Neutron noise observations in German KWU built PWRs and analyses with reactor dynamics code DYN3D. Ann. Nucl. Energy 112, 715−734. https://doi.org/10.1016/j.anucene.2017.10.033.

Rouchon, A., Zoia, A., Sanchez, R., 2017. A new Monte Carlo method for neutron noise calculations in the frequency domain. Ann. Nucl. Energy 102, 465−475. https://doi.org/10.1016/j.anucene.2016.11.035.

Shen, X., Hibiki, T., Nakamura, H., 2015. Bubbly-to-cap bubbly flow transition in a long-26 m vertical large diameter pipe at low liquid flow rate. Int. J. Heat Fluid Flow 52, 140−155. https://doi.org/10.1016/j.ijheatfluidflow.2015.01.001.

Shibata, K., Iwamoto, O., Nakagawa, T., Iwamoto, N., Ichihara, A., Kunieda, S., Chiba, S., Furutaka, K., Otuka, N., Ohsawa, T., Murata, T., Matsunobu, H., Zukeran, A., Kamada, S., Katakura, J., 2011. JENDL-4.0: A new library for nuclear science and engineering. J. Nucl. Sci. Technol. 48(1), 1−30. https://doi.org/10.1080/18811248.2011.9711675.

Talamo, A., Gohar, Y., Yamamoto, T., Yamanaka, M., Pyeon, C.H., 2019. Calculation of the

cross and auto power spectral densities for low neutron counting from pulse mode detectors. Ann. Nucl. Energy 131, 138−147. https://doi.org/10.1016/j.anucene.2019.03.032.

Tsuruta, H., Kobayashi, I., Suzaki, T., Ohno, A., Murakami, K., Matsuura, S., 1978. Critical sizes of light-water moderated UO_2 and PuO_2-UO_2 lattices. Japan Atomic Energy Research Institute, JAERI-1254.

Uhrig, R.E., 1970. Random noise techniques in nuclear reactor systems. The Ronald Press Company, New York.

Valentine, T.E., Mihalczo, J.T., 1996. MCNP-DSP: a neutron and gamma ray Monte Carlo calculation of source-driven noise-measured parameters. Ann. Nucl. Energy 23, 1271-1287. https://doi.org/10.1016/0306-4549(96)00004-7.

Van der Hagen, T.H.J.J., Hoogenboom, J.E., 1988. Fast measurements of the in-core coolant velocity in a BWR by neutron noise analysis. Ann. Nucl. Energy 15, 439−488. https://doi.org/10.1016/0306-4549(88)90043-6.

Vidal-Ferràndiz, A., Carreño, A., Ginestar, D., Demazière, C., Verdú, G., 2020. Neutronic simulation of fuel assembly vibrations in a nuclear reactor. Nucl. Sci. Eng. 194, 1037−1078. https://doi.org/10.1080/00295639.2020.1756617.

Viebach, M., Lange, C., Bernt, N., Seidl, M., Hennig, D., Hurtado, A., 2019. Simulation of low-frequency PWR neutron flux fluctuations. Prog. Nucl. Energy 117, 103039. https://doi.org/10.1016/j.pnucene.2019.103039.

Woodcock, E.R., 1965. Techniques used in the GEM code for Monte Carlo neutronics calculations in reactors and other systems of complex geometry. Argonne National Laboratory, ANL-7050.

Yamamoto, T., 2014. Void transit time calculations by neutron noise of propagating perturbation using complex-valued weight Monte Carlo. Proc. PHYSOR 2014, Kyoto, Japan, Sep. 28-Oct. 3, 2014.

Yamamoto, T., 2015. Higher harmonic analyses of the ^{252}Cf source driven noise analysis

19

method. Ann. Nucl. Energy 76, 521−529. https://doi.org/10.1016/j.anucene.2014.10.034.

Yamamoto, T., Sakamoto, H., 2016. New findings on neutron noise propagation properties in void containing water using neutron noise transport calculations. Prog. Nucl. Energy 90, 58−68. https://doi.org/10.1016/j.pnucene.2016.03.003.

Yamamoto, T., 2017. Time-dependent Monte Carlo simulations for neutron noise in void-containing water flow. Prog. Nucl. Energy 101, 270−278. https://doi.org/10.1016/j.pnucene.2017.08.013.

Yamamoto, T. Sakamoto, H., 2021. Frequency domain Monte Carlo simulations of void velocity measurements in an actual experimental setup using a neutron noise technique. J. Nucl. Sci. Technol. 58(2), 190−200. https://doi.org/10.1080/00223131.2020.1814176.

List of figures

Fig. 1 Configuration of void-containing water flow and neutron detectors
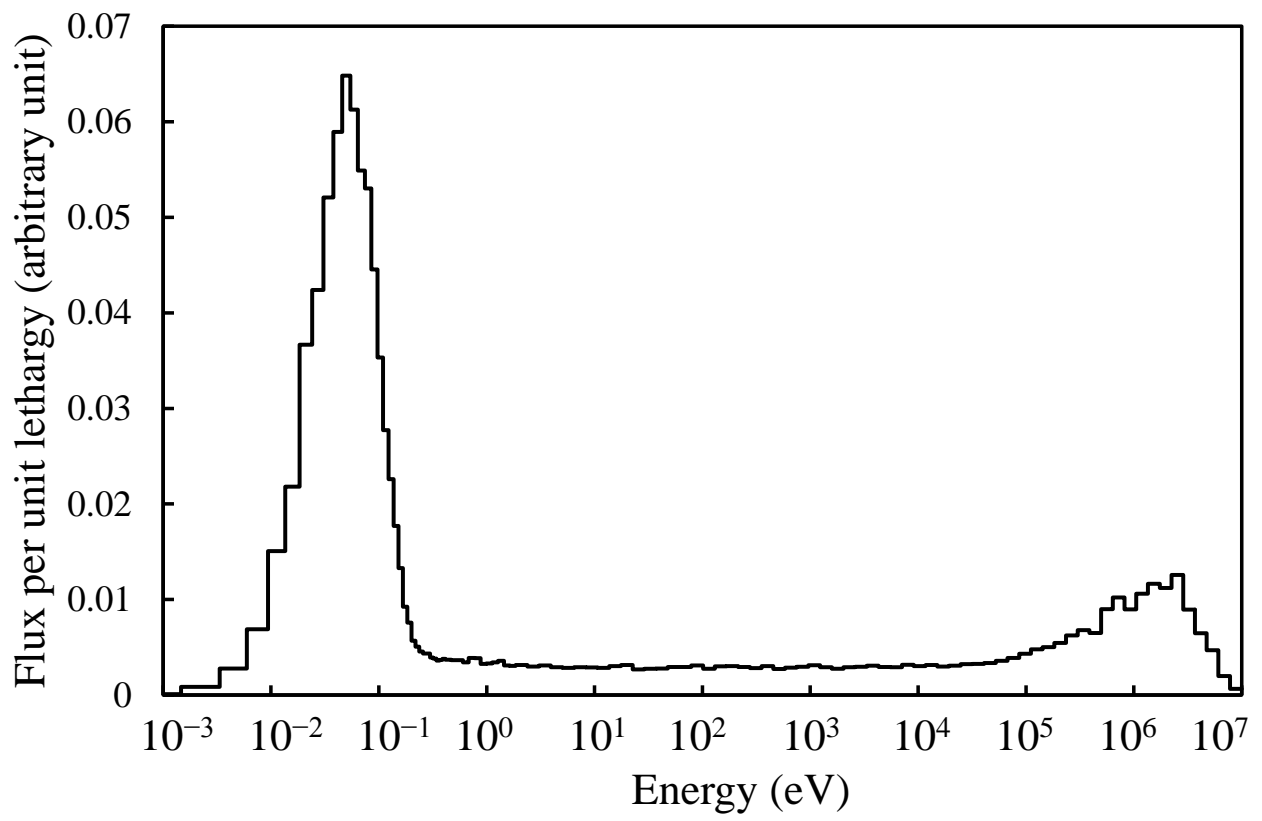
Fig. 2 Neutron spectrum of source neutrons
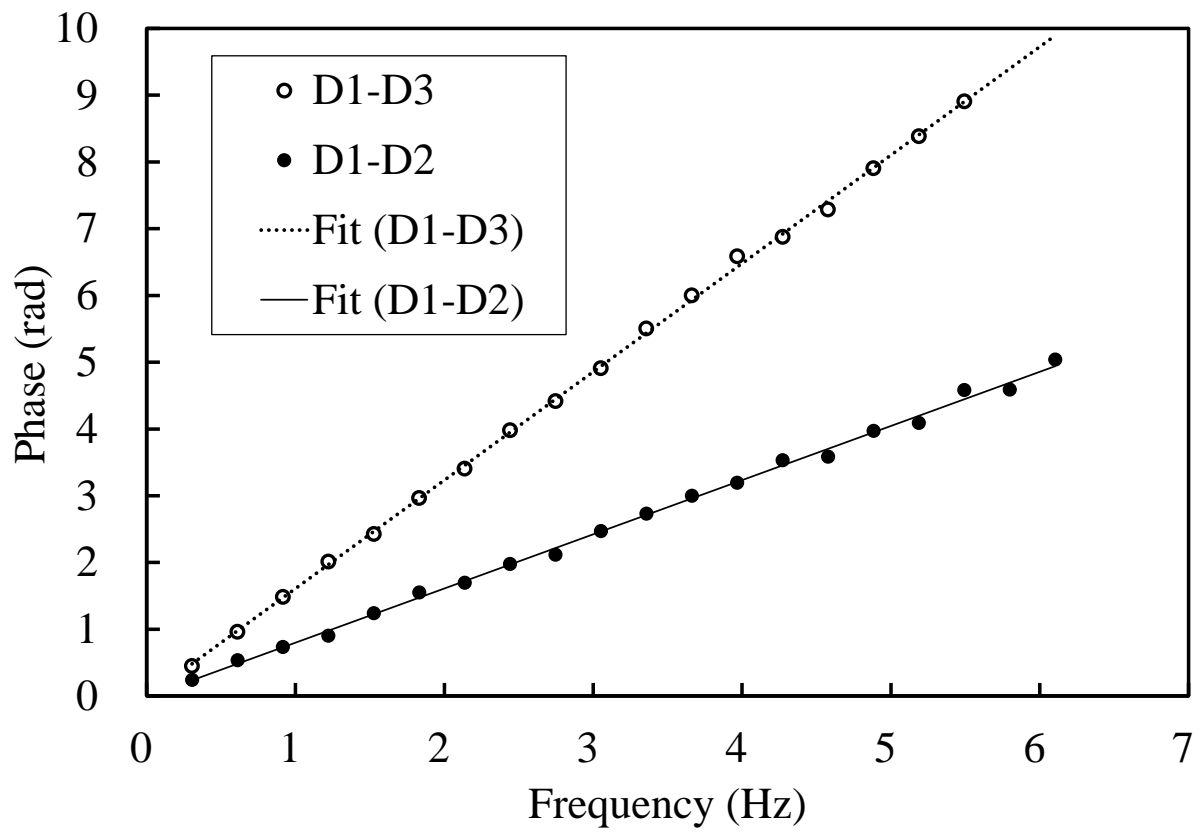
Fig. 3 Phase as a function of frequency in Case 1
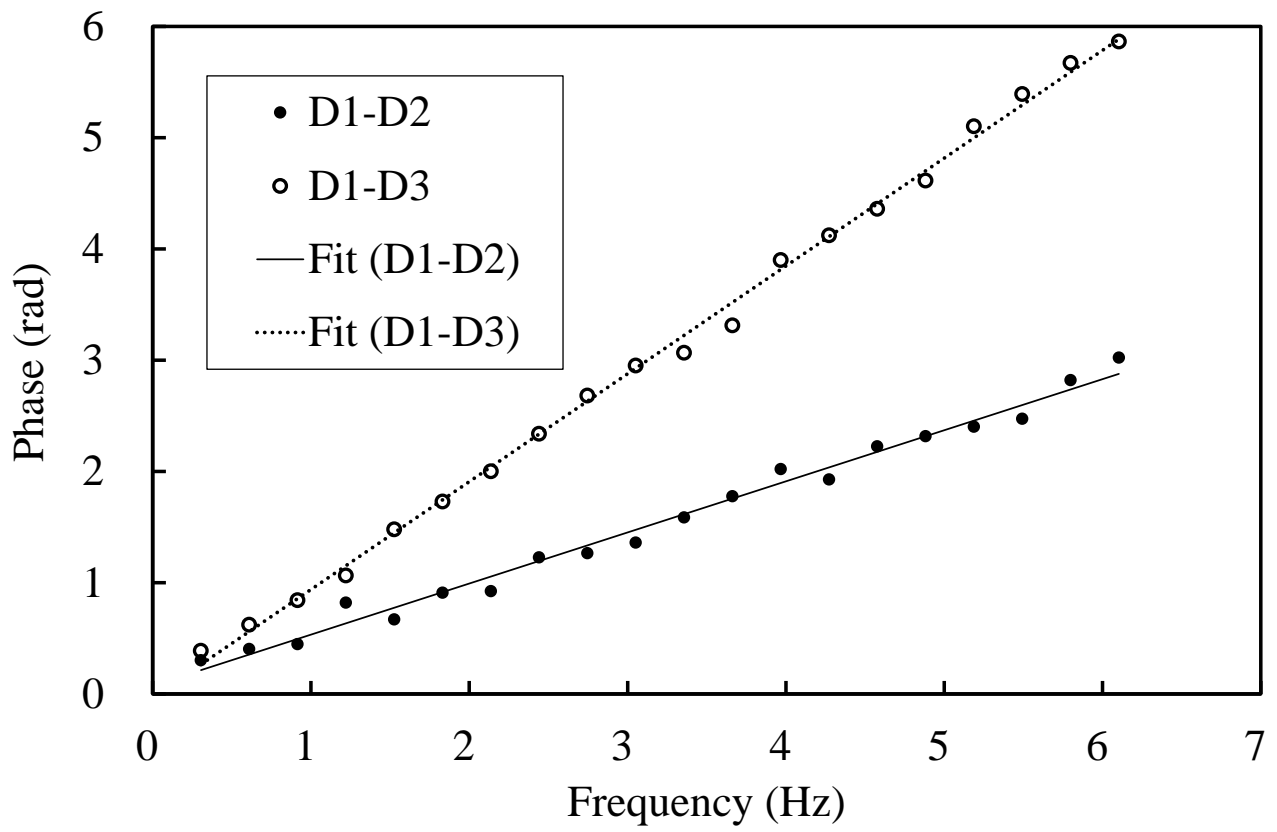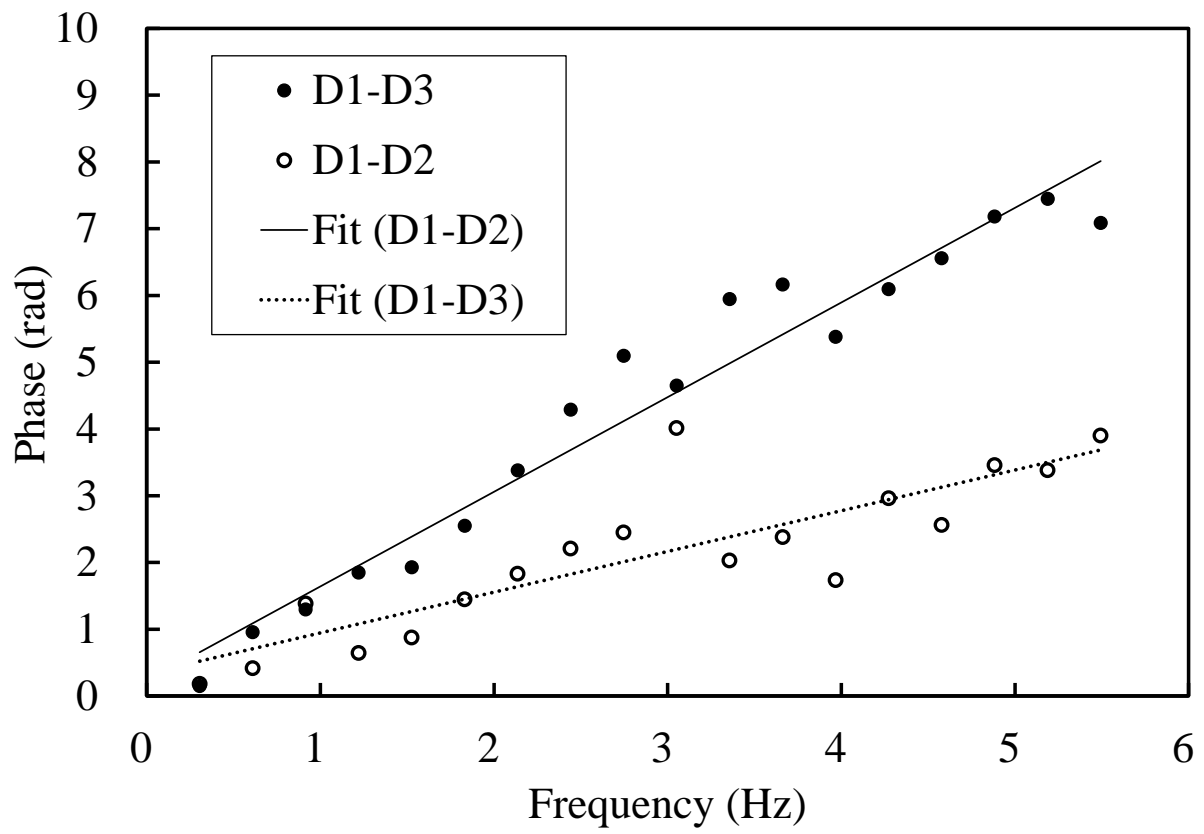
Fig. 4 Phase as a function of frequency in Case 2

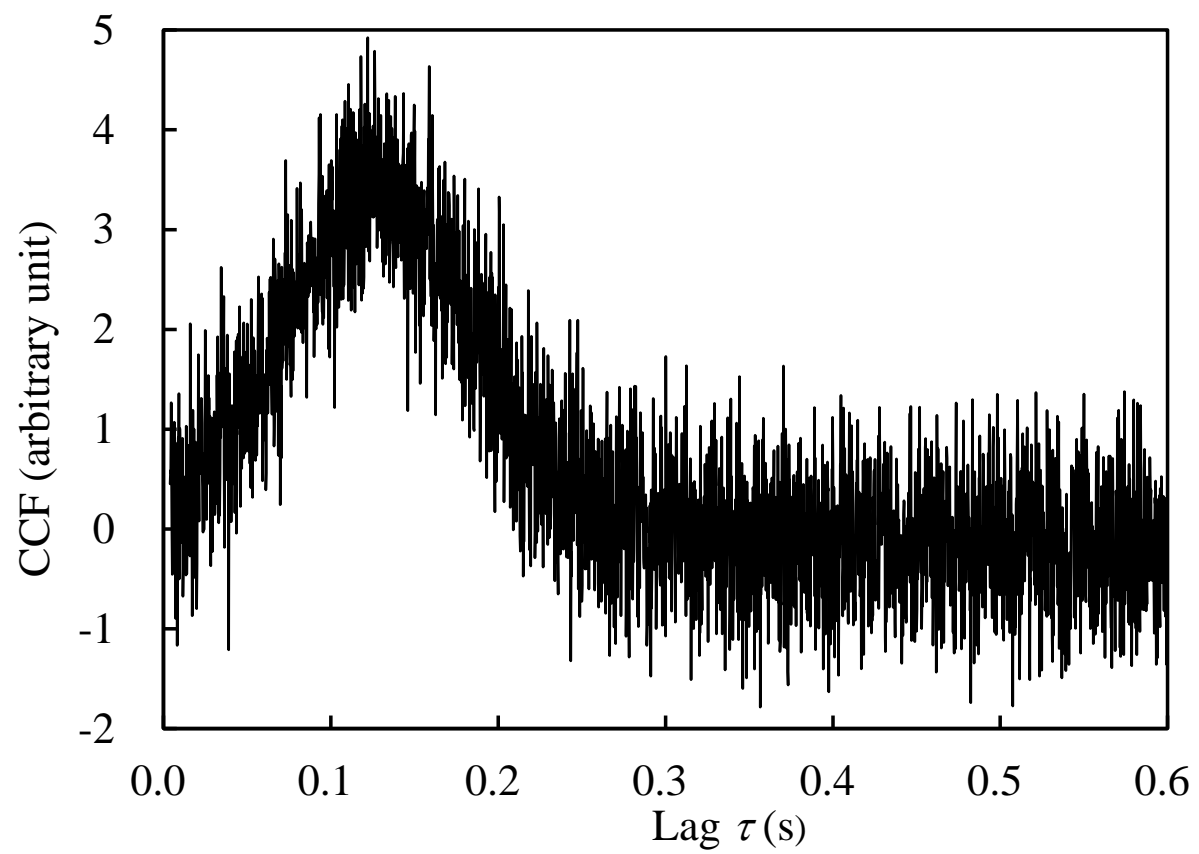Fig. 5 Phase as a function of frequency for $d_B = 0.4$ cm

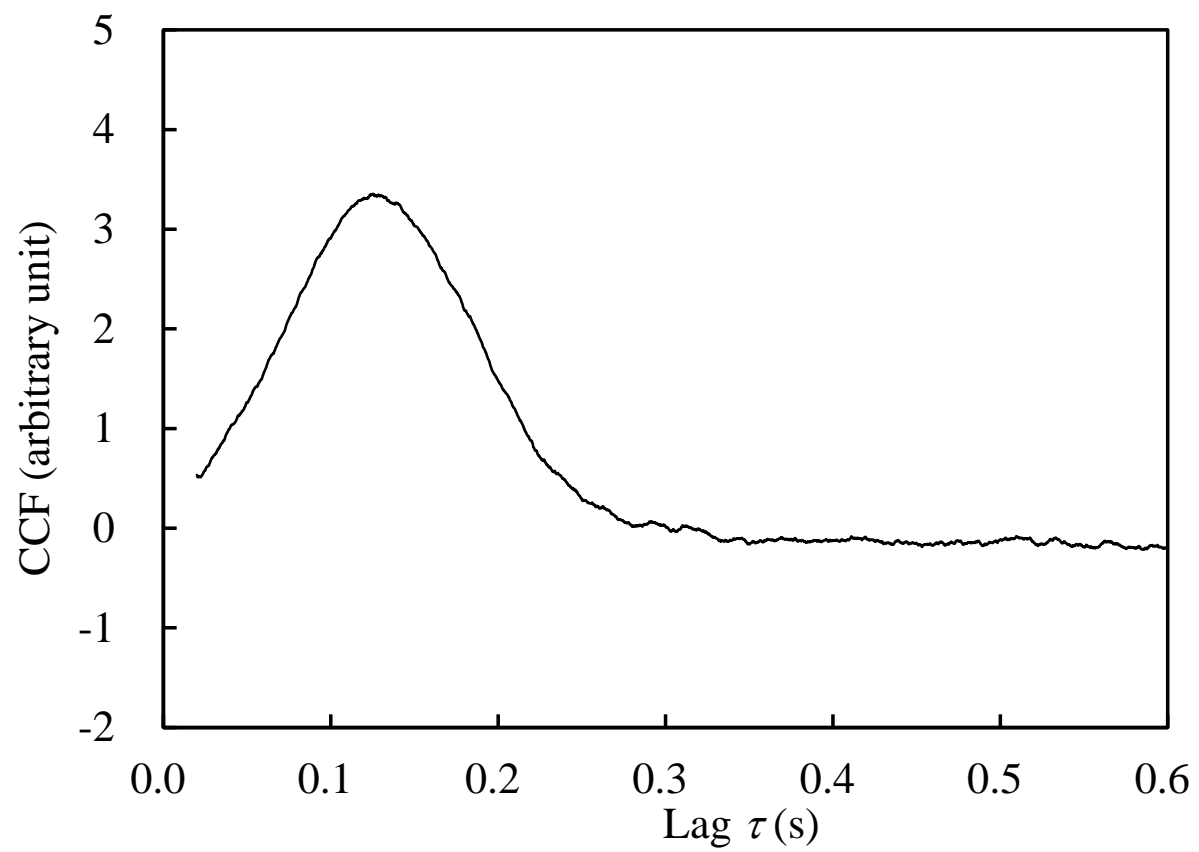Fig. 6(a) CCF in Case 1 as a function of lag τ (G = 5 cm)

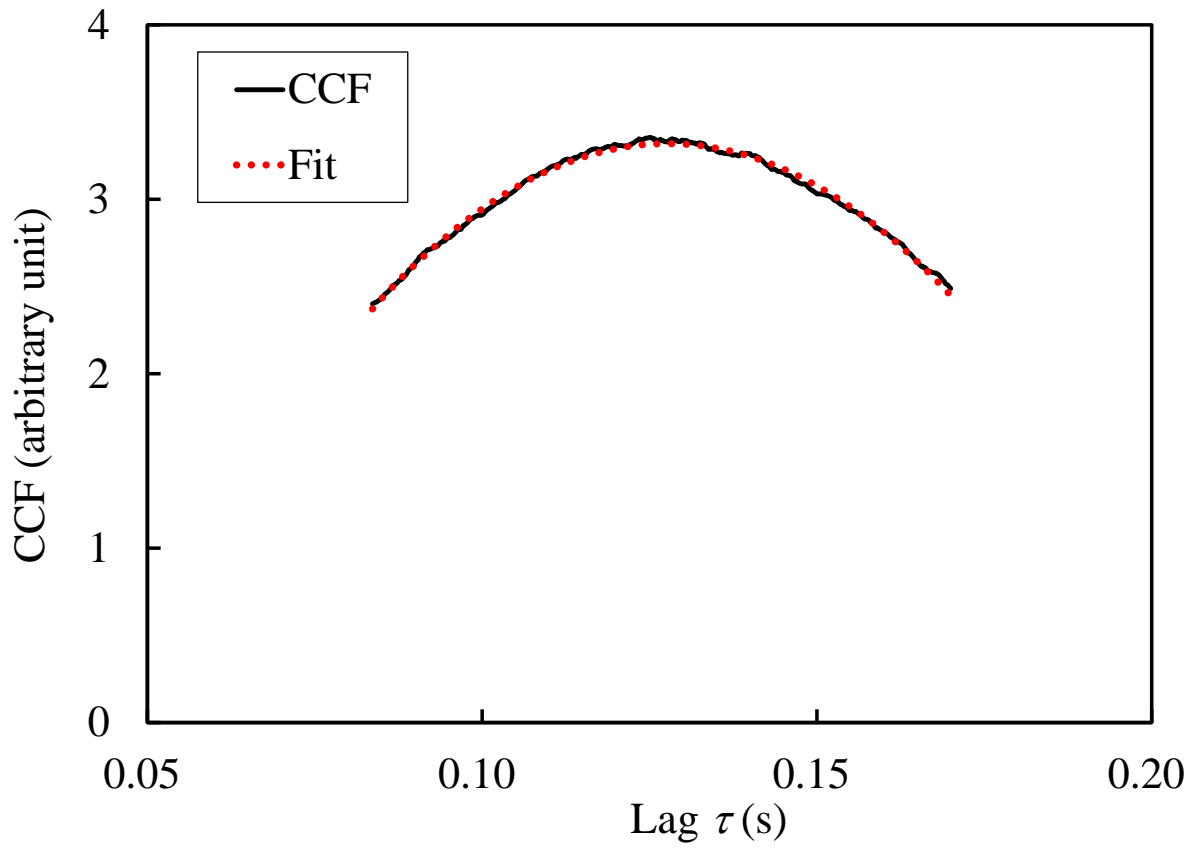Fig. 6(b) Moving average of CCF from Fig. 6(a) ($G = 5$ cm)

Fig. 6(c) Moving average from Fig. 6(b) and fitted quadratic function ($G = 5$ cm)
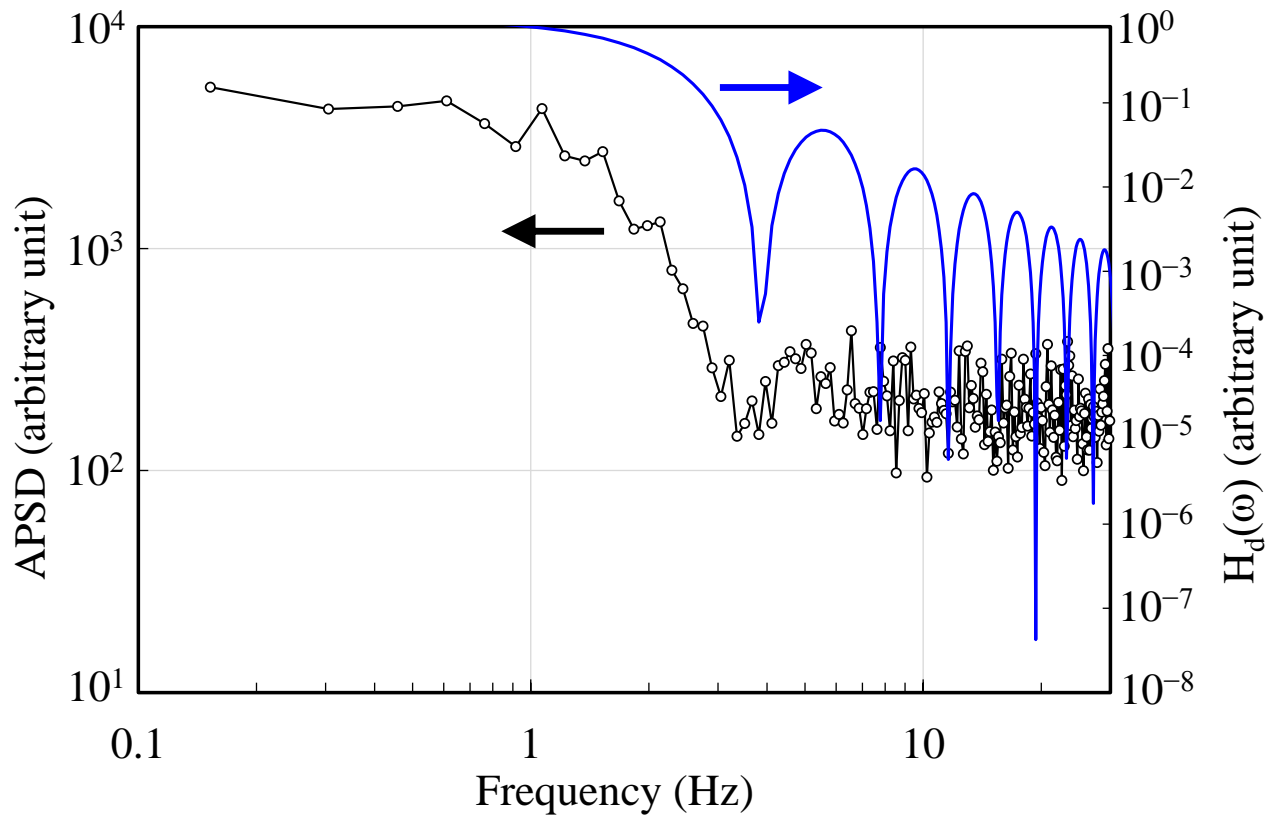
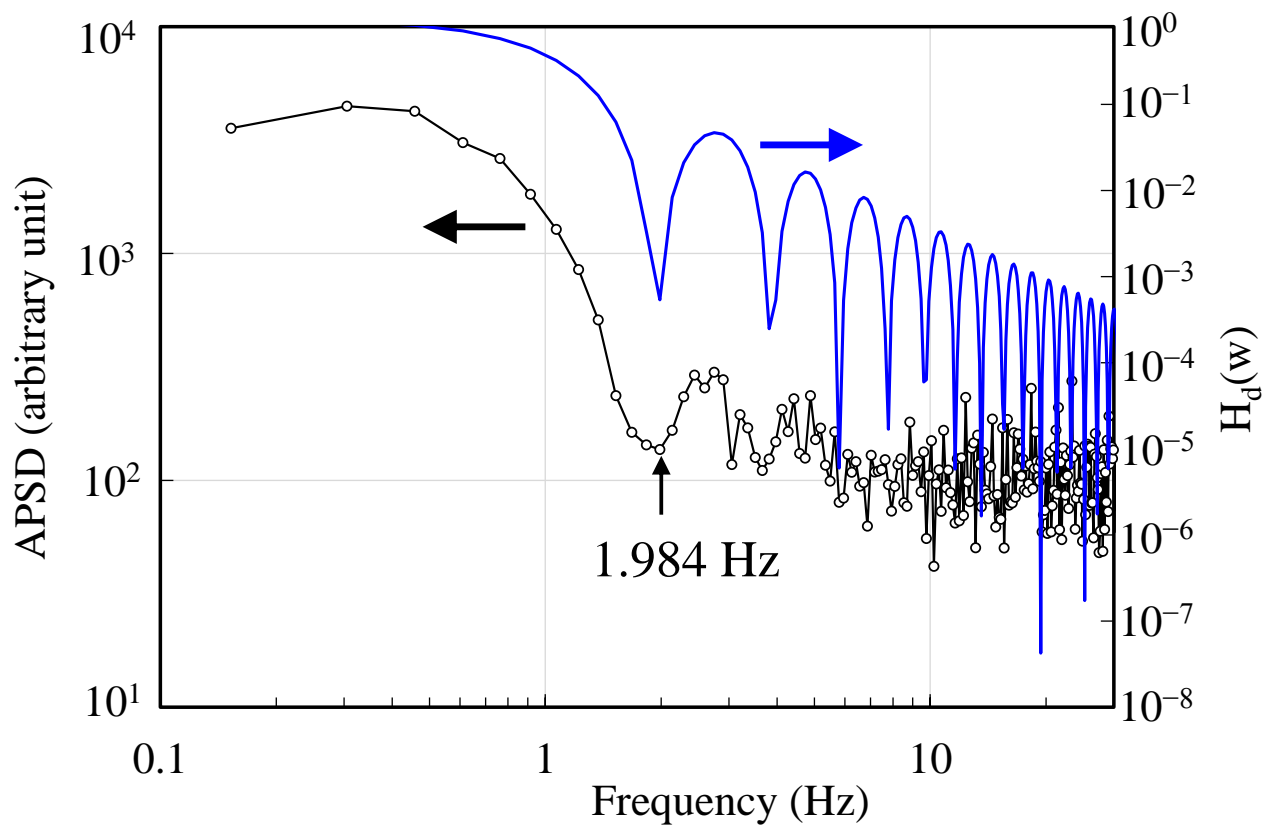Fig. 7 APSD and $H_d(\omega)$ for detector length $L = 20$ cm

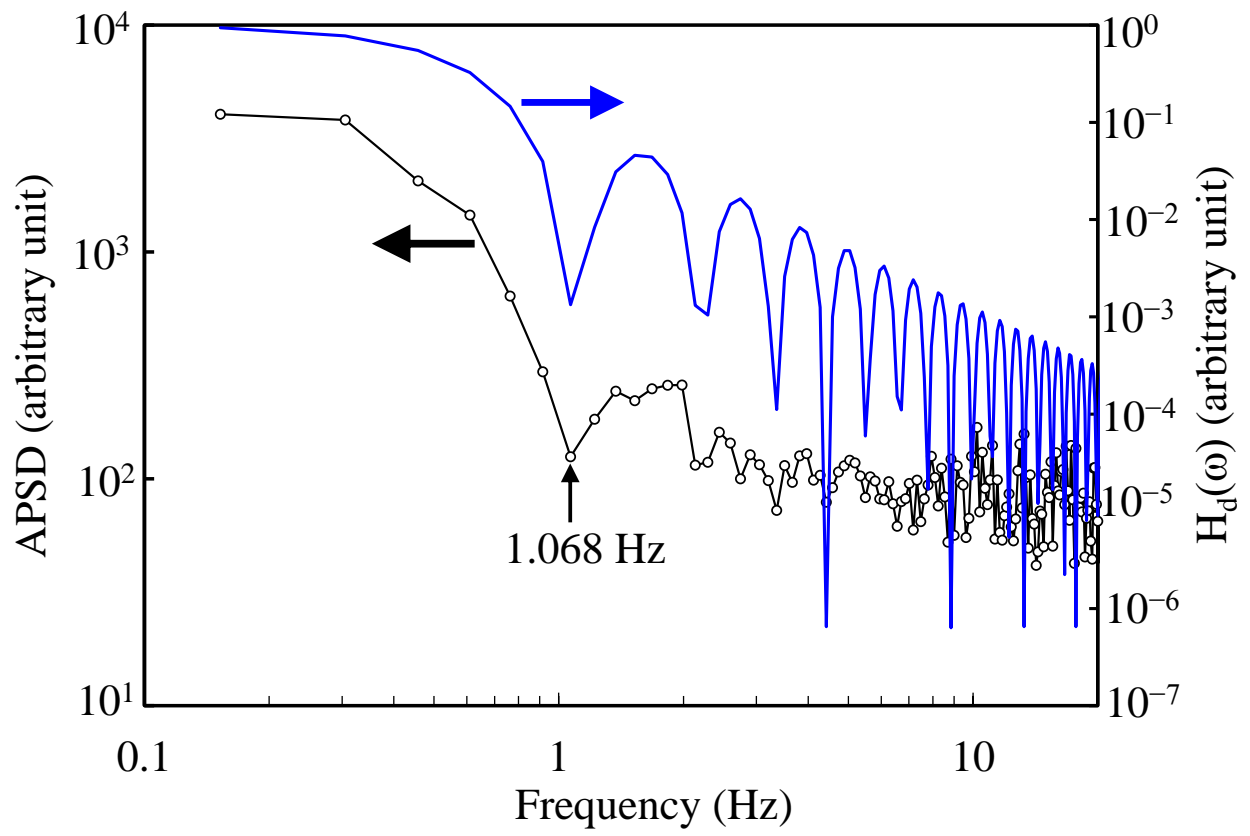Fig. 8 APSD and $H_d(\omega)$ for detector length $L = 40$ cm

Fig. 9 APSD and $H_d(\omega)$ for detector length $L = 70$ cm

Table 1 Void velocity by CPSD

No.	Void fraction α (%)	Bubble diameter d_B (cm)	G (cm)	Void velocity V_g (cm/s)	Void velocity (cm/s)		
					D1-D2	D2-D3	D1-D3
1	5.3	0.910	5	77.5	77.7 ± 0.4	77.5 ± 0.6	77.6 ± 0.2
2	13.18	0.809	5	129.6	131.7 ± 1.2	131.0 ± 1.6	130.6 ± 0.9
3	13.18	0.809	10	129.6	129.7 ± 0.8	129.7 ± 1.1	130.4 ± 0.6
4	5.3	0.4	5	77.5	89.9 ± 5.7	70.3 ± 6.1	81.8 ± 2.4

Table 2 Void velocity by CCF

No.	Void fraction α (%)	Bubble diameter d_B (cm)	G (cm)	Void velocity V_g (cm/s)	Void velocity (cm/s)		
					D1-D2	D2-D3	D1-D3
1	5.3	0.910	5	77.5	78.3 ± 0.3	77.0 ± 0.4	77.6 ± 0.3
2	13.18	0.809	5	129.6	126.4 ± 0.7	127.6 ± 0.5	130.4 ± 0.6
3	13.18	0.809	10	129.6	130.3 ± 0.6	130.1 ± 0.5	129.3 ± 0.4

Declaration of interest statement

The authors declare no conflicts of interest associated with this manuscript.